Rheology and DWS microrheology of concentrated suspensions of the semiflexible filamentous fd virus

E. Sarmiento-Gomez, D. Montalvan-Sorrosa, C. Garza, J. Mas-Oliva and R. Castillo

Regular Article

Rheology and DWS microrheology of concentrated suspensions of the semiflexible filamentous fd virus

E. Sarmiento-Gomez[1], D. Montalvan-Sorrosa[1], C. Garza[1], J. Mas-Oliva[2], and R. Castillo[1,a]

[1] Instituto de Fisica, Universidad Nacional Autónoma de Mexico, P. O. Box 20-364, Mexico D. F. 01000
[2] Instituto de Fisiología Celular, Universidad Nacional Autónoma de Mexico, P. O. Box 20-364, Mexico D. F. 01000

Abstract. Microrheology measurements were performed on suspensions of bacteriophage fd with diffusive wave spectroscopy in the concentrated regime, at different values of ionic strength. Viscosity *vs.* shear rate was also measured, and the effect of bacteriophage concentration and salt addition on shear thinning was determined, as well as on the peaks in the viscosity *vs.* shear curves corresponding to a transition from tumbling to wagging flow. The influence of concentration and salt addition on the mean square displacement of microspheres embedded in the suspensions was determined, as well as on their viscoelastic moduli up to high angular frequencies. Our results were compared with another microrheology technique previously reported where the power spectral density of thermal fluctuations of embedded micron-sized particles was evaluated. Although both results in general agree, the diffusive wave spectroscopy results are much less noisy and can reach larger frequencies. A comparison was made between measured and calculated shear modulus. Calculations were made employing the theory for highly entangled isotropic solutions of semiflexible polymers using a tube model, where various ways of calculating the needed parameters were used. Although some features are captured by the model, it is far from the experimental results mainly at high frequencies.

1 Introduction

Many of the diverse material properties observed in fluid soft materials are related to the complex supramolecular structures embedded in them, as is the case of suspensions of wormlike micelles, F-actine, and filamentous viruses, where their threadlike or filamentous structures form an entangled network that introduces a complex dynamics, usually described with multiple characteristic lengths and time scales, which are analogous to those used in polymers. Typical characteristic lengths are filament diameter d, contour length L_c, persistence length l_p, mesh size ξ, and entanglement length l_e. The ratio between L_c and l_p provides a criterion to distinguish between two asymptotic classes of these threadlike structures, the flexible ones $(L_c \gg l_p)$ and the rigid-rod ones $(L_c \ll l_p)$. Whereas the viscoelastic behavior of dilute and concentrated entangled solutions of flexible and rod like polymeric threadlike structures is fairly well understood [1], there is no qualitatively correct description of the viscoelasticity of solutions of semiflexible polymeric threadlike structures over the whole range of concentrations. This is the case of the filamentous fd bacteriophage suspension, which provides an excellent model of a network made of monodisperse semiflexible filaments, $L_c \sim l_p \gg d$. The fd virus is a

rod-shaped virus constituted by a single-stranded circular DNA covered with a protein coat. This protein cover consists of a helical shell of ~ 2700 identical α-helical protein subunits (~ 50 aminoacids) wrapped following a 5-fold rotation axis combined with a 2-fold screw axis, associated to ten proteins capping each one of the two ends [2–6]. This filament has a contour length of $L_c \sim 900$ nm, with a diameter $d_{\rm fd} \sim 7$ nm, and a persistence length of $l_p \sim 2200$ nm; as a consequence, the aspect ratio of fd $\varepsilon = L_c/d_{\rm fd} \sim 130$; fd molecular mass is $MW_{\rm fd} \sim 1.64 \times 10^7$ Da. On its surface there are located ~ 9000 ionizable groups that in aqueous solutions at neutral pH can reach a charge density of about $9\,{\rm e/nm}$ [7]; in highly deionized water, this leads to long-range Coulomb interaction. The fd virus isoelectric point is at pH $= 4.2$, above which the virus surface is negative, while being positive below [7]. The overlap concentration $c^* \sim 1$ particle/$L_c^3 \sim 0.04\,{\rm mg/mL}$. The equilibrium phase behavior of the fd virus differs from the ideal hard rod. The finite flexibility of the virus drives the concentration of the bimodal points to higher values when compared to equivalent, but perfectly stiff hard rods, and also reduces the value of the order parameter of the coexisting nematic phase. The effect of the surface charge is to increase the effective diameter of the rod, and therefore the excluded-volume interaction between charged rods. As

a e-mail: rolandoc@fisica.unam.mx

a consequence, the charge reduces the real concentration of the phase transition.

The rheological response of soft materials can be linear or nonlinear depending on the applied stress. Nonlinearity is usually a sign of structural rearrangement in the system by the applied stress or deformation. For systems close to thermodynamic equilibrium, there is always a linear response regime for small enough applied strain or stress. In soft materials, one of the most important properties is the shear modulus, G, which connects the deformation and flow of materials in response to applied stresses, $\sigma = \int_{-\infty}^{t} dt' G(t-t') \dot{\gamma}$. Here, σ is the shear stress and $\dot{\gamma}$ is the shear rate. In contrast with other materials, like simple liquids or solids, the shear modulus in soft materials exhibit a significant time (or frequency through $G^*(\omega) = i\omega \int_0^\infty G(t) e^{-i\omega t} dt$) dependence in the range of milliseconds to seconds, or even to minutes. In essence, soft materials are viscoelastic, *i.e.*, they exhibit both a viscous and an elastic response. Upon application of an oscillatory shear strain at a frequency ω, the real part of $G^*(\omega)$, *i.e.*, the storage modulus $G'(\omega)$ is in phase with the applied shear strain. The imaginary part of $G^*(\omega)$, the viscous or loss component of the stress, $G''(\omega)$, is in phase with the shear rate $\dot{\gamma}$. Regularly, $G^*(\omega)$ is determined using mechanical rheometers, where viscoelastic properties are measured by application of a strain while measuring stress or vice versa. However, in the last fifteen years different techniques have been developed, usually named microrheology techniques, where micron-sized probe particles are embedded into the fluid to locally measure the viscoelastic response of soft materials [8]. This response can be measured either by actively manipulating the probe particles or by passively measuring their mean square displacement, $MSD = \langle \Delta r^2(t) \rangle$, where the bulk mechanical susceptibility of the fluid determines the response of these probe particles, which are excited by the thermal stochastic forces leading to Brownian motion. $\langle \Delta r^2(t) \rangle$ can be related to $G^*(\omega)$ by describing the motion of the particles with a generalized Langevin equation incorporating a memory function, to take into account the viscoelasticity of the fluid. In this way, the particle fluctuation can be used to measure the relaxation spectrum of the fluid. Here, in contrast to mechanical rheometers, there is no strain applied on the material during the measurement, something particularly useful in soft materials, where even small imposed strains can cause structural reorganization of the material, and consequently a change in their viscoelastic properties.

fd bacteriophage suspensions are quite attractive soft materials, because they form liquid crystals at specific ranges of concentration and ionic strength [9,10]; a review can be found in ref. [11]. These suspensions with rodlike colloids also present a complex nonlinear rheology, because orientation is strongly coupled to the shear field [12–16]. Rods in the isotropic (I) phase align with the flow and become paranematic (P). An isotropic state under flow is referred to as a paranematic state to indicate that flow partially aligns otherwise isotropic rods. The location of the isotropic (paranematic)-nematic phase transition is modified because shear flow strongly aligns rods.

Besides, in the presence of shear flow, rods in the nematic phase can undergo a collective tumbling motion. In addition, shear flow leads to the formation of banded structures in fd virus suspensions, which exhibit shear- and vorticity-banding [12–16]. The linear viscolastic properties of suspensions of fd bacteriophage have been measured by Schmidt *et al.* [17] using both mechanical rheometry and active microrheology employing a magnetic tweezers rheometer and particle tracking. This study was mainly addressed to get $G'(\omega)$ and $G''(\omega)$ in the low-frequency range ($\sim 0.06 < \omega < 25\,\text{rad/s}$) for suspensions in a concentration, c, range of 5–15 mg/mL, with a fixed ionic strength ($I = 100\,\text{mM}$). $G''(\omega) > G'(\omega)$ for all frequencies below 6.2 rad/s. At frequencies above 6.2 rad/s, a shallow and slanted plateau-like region was found for $G'(\omega)$, where $G'(\omega) \sim G''(\omega)$. $G''(\omega)$ exhibits a small inflection point at $\omega \sim 6.2\,\text{rad/s}$. At low frequencies, according to theory [18] a behavior of the form $G' \sim \omega^2$ and $G'' \sim \omega^1$ was expected, because suspensions of semiflexible filaments behave more like rigid rods, since the undulatory excitations are completely damped out; nevertheless, it was found [17] that $G' \sim \omega^{0.9\text{-}1.2}$ and $G'' \sim \omega^{0.7\text{-}0.9}$.

In addition, zero shear viscosity, η_0, was calculated from $G''(\omega)/\omega$. However, it was found that $\eta_0 \sim c^{2.6}$; although, $\eta_0 \sim c^3$ was expected, as in the case of rigid rods. Previously, Graf *et al.* [19] reported that viscosity, η, in fd suspensions increases with the virus concentration due to the Coulomb interaction between the rods, *i.e.*, when the Debye length in the suspension is in the order of the typical interparticle distance. They also found that when the ionic strength increases the viscosity decreases. The authors also showed that the specific viscosity follows certain power laws on concentration, and they found that as the shear rate increased, the viscosity decreased steadily at constant ionic strength, I, in the considered range of concentration ($0.04\,\text{mg/mL} \sim 1c^*$ to $9.12\,\text{mg/mL} \sim 228c^*$, and $I = 100\,\text{mM}$). They never observed peaks in the η *vs.* $\dot{\gamma}$ diagrams as in [13]. Addas *et al.* [20] studied fd virus suspensions from the dilute to the concentrated regime ($c \sim 0.2$–14 mg/mL) at $I = 50\,\text{mM}$, and $pH = 7$. $G'(\omega)$ and $G''(\omega)$ were measured evaluating the power spectral density of the thermal fluctuations of embedded micronsized silica particles. Here, a focused laser beam was used to trap the microspheres, and interferometric photodiode detection was used to measure passively the position fluctuations of the trapped microspheres with nanometer resolution and high bandwidth ($0.62 < \omega < 6.2 \times 10^4\,\text{rad/s}$). In the dilute regime these authors found that $G^*(\omega)$ is dominated by the rigid-rod rotational relaxation. Increasing the fd concentration, both moduli increase and, relatively, the elastic character of the suspension increases. Just below the isotropic-nematic phase transition, the elastic modulus is $\sim 10\,\text{Pa}$, and the sample is still mainly viscous, *i.e.*, it remains rather weakly entangled. This was attributed to the relative short virus contour length and to its charged surface, which prevents sticking between them. In the high-concentration regime, at high frequencies, suspensions apparently reflect a single semiflexible filament dynamics; $G''(\omega) \sim \omega^{3/4}$ as predicted for semiflexible polymers. Rhe-

ology of modified fd virus made by grafting the polymer poly(N-isopropylacrylamide) to the virus surface has also been studied, this system can be treated as colloidal rods interacting with a temperature-dependent attraction [21, 22].

The theory developed for tightly entangled isotropic solutions of semi-flexible polymers developed by Morse [18,23,24] has been used to understand the linear rheological properties of high concentrated fd virus suspensions. Here, each polymer is confined on short time scales within a tube of diameter, $D_e \ll l_p$. Free motions along the tube contour are hindered only by the viscous dissipation due to the solvent. The shape of the tube deforms affinely in response to macroscopic deformation of the solution, and excluded-volume interactions between polymers are neglected except for keeping the polymer in its tube. The linear complex modulus of a solution of long, tightly entangled chains is dominated at low frequencies by a curvature contribution to the stress, analogous to the elastic stress of entangled flexible chains, which relaxes by reptation and gives rise to a broad elastic plateau. At higher frequencies, the modulus is dominated by a larger tension contribution, whose frequency dependence is controlled at intermediate frequencies by the diffusion of the excess length along the tube. Because the tube has a nonzero diameter, small transverse ondulations of the polymer within the tube are allowed, and the dynamics of these ondulation modes control the high-frequency response of the model. Therefore, at very high frequencies the modulus is dominated by the unhindered transverse motion of the chain within the tube. This high-frequency regime yields a complex modulus that varies as $G^*(\omega) \sim (i\omega)^{3/4}$. The calculated moduli have to be corrected to include the bare solvent contribution by adding $i\omega\eta_s$, where η_s is the solvent viscosity.

The aim of this work is to re-examine the viscoelastic properties of suspensions made of filamentous fd bacteriophage, particularly in the high concentrated regime and at different values of the ionic strength. The viscosity *vs.* shear rate, $\dot{\gamma}$, in these suspensions was measured, and the influence of virus concentration and salt addition was determined on the shear thinning as $\dot{\gamma}$ increases, as well as on the peaks in the η *vs.* $\dot{\gamma}$ curves corresponding to a transition from tumbling to wagging flow. Furthermore, the influence of concentration and salt addition on the MSD of microspheres embedded in virus suspensions, and on the viscoelastic moduli up to very high frequencies, was determined employing a multiple scattering technique, diffusive wave spectroscopy (DWS). The viscoelastic moduli were compared with the results obtained by Addas *et al.* [20] who get those properties evaluating the power spectral density of the thermal fluctuations of embedded micron-sized particles, and with results of mechanical rheology. The viscoelastic moduli of the suspensions were evaluated using the model developed by Morse [18, 23,24] for tightly entangled isotropic solutions of semi-flexible polymers. These calculations were compared with our DWS experiments. As we will present later, Morse's model captures some experimental features, although it is

qualitatively far from the experimental values when they are compared in a wide angular frequency range. We found two specific drawbacks. The model is not consistent with the Kramer-Kronig (KK) integral relations, and the model does not predict a change in the power law of $G^*(\omega)$ at high frequencies, which is clearly observed in the experiments.

2 Experimental section

Materials and methods. fd virus was prepared using standard microbiological methods [25]. We used the XL1-Blue strain of *Escherichia coli* as host bacteria. Bacteria batches were obtained and infected with the fd bacteriophage. Bacteria were separated from the media by using low-speed centrifugation. The virus was precipitated with polyethylene glycol (PEG 8000). A purified sample of virus was obtained after multiple resuspension and sedimentation steps by ultracentrifugation. The final pellet was resuspended and extensively dialyzed against 20 mM Tris-HCl buffer at $pH = 8.15$, and sodium azide was added to prevent bacterial growth (1 mM). The stock suspension was diluted to obtain the needed virus concentration and salt was added to fix the needed [NaCl] concentrations. Samples were placed in sealed containers to avoid water evaporation, and heated at 40 °C to reduce viscosity. Then, negative charged polystyrene microspheres of a diameter of 2 μm in water suspension (10 w% Bangs Labs Inc. IN, USA) were added while stirring the samples. Stirring was maintained for 15 min to assure a homogeneous dispersion. To avoid interparticle interactions, as well as hydrodynamic correlation, microsphere volume fractions, φ, were kept low ~ 0.03.

Rheology. Mechanical rheometric measurements were performed in a Bohlin Gemini HRnano rheometer (Malvern Instruments, UK). All dynamic viscoelastic spectra measurements were done using cone-plate geometry (4°– 40 mm). Measurements were made a day after the solution preparation to allow them to reach equilibrium.

Atomic force microscopy (AFM). Dilute fd suspensions deposited on freshly cleaved mica were scanned with a scanning probe microscope (JSTM-4200 JEOL, Japan) with a 10 μm × 10 μm scanner in air and at high vacuum (10^{-4} Pa). Noncontact cantilevers with a nominal force constant of 5.7 N/m (HI RES/AlBS, MikroMasch, Estonia) were used, which have diamond-like spikes (tip radius < 1 nm) on the apex of the silicon tip, mounted on a rectangular silicon chip with Al backside coating. Topographic and phase images were obtained by using the dynamic mode (AC mode). Here, the cantilever is externally oscillated close to its fundamental resonance. The changes in the oscillation amplitude of the cantilever, or phase lag of the cantilever oscillation relative to the signal sent to the cantilever's piezo-driver, provide the feedback signal for imaging, *i.e.*, a z-scanner controller moves the sample along the vertical direction such that the oscillation amplitude and phase of the vibrating cantilever stays at a fixed value (intermittent contact or tapping mode).

Transmission electron microscopy (TEM). Dilute fd suspensions were deposited on carbon-coated TEM grids. Most of the solution was removed by blotting with the edge of a filter paper. Afterward, a solution made of 2% uranyl acetate for negative staining was applied, and the samples were dried again. Microstructural analysis the specimens was performed in a TEM JEM-1200EX11 (JEOL, Japan).

Diffusive wave spectroscopy (DWS). DWS is a multiple scattering technique that probes particle motion over length scales much shorter than the wavelength of light in the scattering medium, λ. In conventional dynamic light scattering (DLS) in the single scattering limit, the characteristic time dependence of the fluctuations is determined by particle motion over a length scale set by the inverse wave vector $q^{-1} \sim \lambda$, where $q = (4\pi/\lambda)\sin(\theta/2)$ and θ is the scattering angle. In the multiple scattering regime, the characteristic time dependence is determined by the cumulative effect of many scattering events and, thus, by particle motion over length scales much less than λ. Therefore, the characteristic time scales are much faster and the corresponding characteristic length scales are much shorter than for conventional DLS. As a consequence, DWS can allow us to reach microrheology at high frequencies, which is not possible with DLS.

Our DWS setup is a home-made instrument described elsewhere [26]. In DWS, the Brownian motion of probe particles incorporated in the fluid of interest is followed with multiple dynamic light scattering; the particles in the fluid are in a concentration that makes it turbid. Here, photons are multiply scattered and lose their q-dependence. This leads to instruments using only transmission or back-scattering geometries. DWS connects the temporal electric field fluctuations of the scattered light emerging from the turbid suspension, characterized by the time-averaged field autocorrelation function (ACF), $g^{(1)}(t) = \langle E(0)E^*(t)\rangle/\langle|E(0)|^2\rangle$, to the motion of the particles incorporated in the fluid. That is, the MSD of the probe particles can be determined by collecting the scattered intensity from a single speckle of scattered light, over a sufficiently long collection period, to allow the evaluation of the time-averaged light intensity ACF, $g^{(2)}(t)$. This measured ACF is related to $g^{(1)}(t)$ through the Siegert relation: $|g^{(2)}(t)| = 1 + \beta|g^{(1)}(t)|^2$, where β is an instrumental factor determined by the collection optics. When all the scattering particles suspended in the fluid are free to explore the same local environment during the course of a measurement, the scattering process is ergodic, and time-averaged $(\langle\ldots\rangle_T)$ and ensemble-averaged $(\langle\ldots\rangle_E)$ correlation functions are identical. In a transmission geometry, the fluid under investigation with the scattering particles immersed in it can be treated as a slab with an infinite transverse extent and a thickness $L \gg l^*$, where l^* is the transport mean free path. After traveling a l^* distance, light propagation is randomized, and the transport of light in a turbid medium can be described by the diffusion approximation [27–29]. In this case, the expression of the time averaged field ACF, $g^{(1)}(t)$ is [27–29]

$$g^{(1)}(t) = \frac{\frac{L/l^* + 4/3}{\alpha^* + 2/3}\left(\sinh[a^*x] + \frac{2}{3}x\cosh[a^*x]\right)}{\left(1 + \frac{4}{9}x^2\right)\sinh\left[\frac{L}{l^*}x\right] + \frac{4}{3}x\cosh\left[\frac{L}{l^*}x\right]}, \quad (1)$$

where $x = [k_0^2\langle\Delta\boldsymbol{r}^2(t)\rangle]^{1/2}$ and $\alpha^* = \frac{z_0}{l^*}$. z_0 is the distance into the sample from the incident surface to the place where the diffuse source is located. If l^* is known in the sample, $\langle\Delta\boldsymbol{r}^2(t)\rangle$ can be obtained by using eq. (1). The ability to store energy upon deformation changes the temporal correlations of the stochastic forces acting on the particle at thermal equilibrium, since the suspending medium must satisfy the fluctuation dissipation theorem. In this method, it is assumed [30–33] that the Maxwellian fluid time-dependent memory function, $\zeta(t)$, which accounts for both the energy loss and storage upon deformation, is proportional to the bulk-frequency-dependent viscosity of the fluid, $\tilde{\eta}(s) = \tilde{\zeta}(s)/6\pi a$; this is a generalization of the Newtonian fluid behavior. The relation between $\tilde{G}(s)$ and $\langle\Delta\boldsymbol{r}^2(t)\rangle$ can be written as [32]

$$\tilde{G}(s) = s\tilde{\eta}(s) = \frac{s}{6\pi a}\left[\frac{6k_BT}{s^2\langle\Delta\tilde{\boldsymbol{r}}^2(s)\rangle} - ms\right]. \quad (2)$$

Here, k_B is Boltzmann's constant, s is the frequency in the Laplace domain, and a is the particle radius. Using the unilateral Fourier transform, F_u, an expression for the viscoelastic modulus as a function of frequency can be written as [32]

$$G^*(\omega) = G'(\omega) + iG''(\omega) = \frac{k_BT}{\pi a i\omega F_u[\langle\Delta\boldsymbol{r}^2(t)\rangle](\omega)}. \quad (3)$$

Several procedures have been followed by different authors [32–35] to determine F_u. In our case, numerical inversion of eq. (1) allowed us to obtain $\langle\Delta\boldsymbol{r}^2(t)\rangle$. Instead of making any transformation to $\langle\Delta\boldsymbol{r}^2(t)\rangle$ curve, we first fitted the curve to a model curve proposed by Bellour *et al.* [36], for describing the $\langle\Delta\boldsymbol{r}^2(t)\rangle$ of colloidal particles in Brownian motion embedded in a complex fluid, over several decades in time. This method has been successfully used in the case of wormlike micelles [26,36,37]. The model curve is given by

$$\langle\Delta\boldsymbol{r}^2(t)\rangle = 6\delta^2\left(1 - e^{-\left(\frac{D_0}{\delta^2}t\right)^\alpha}\right)^{1/\alpha}\left(1 + \frac{D_m}{\delta^2}t\right). \quad (4)$$

This model was originally thought for Brownian particles harmonically bound around a stationary mean position, as a consequence $\langle\Delta\boldsymbol{r}^2(t)\rangle = 6\delta^2(1 - e^{-\left(\frac{D_0}{\delta^2}t\right)})$, where the particle's amplitude of the motion, the cage size δ, is related to the elastic modulus $G_0(\delta^2 = k_BT/[6\pi aG_0])$, which does not depend on ω; this result can be obtained substituting this particular $\langle\Delta\boldsymbol{r}^2(t)\rangle$ in eq. (2). However, this cage where particles are momentarily trapped fluctuates. Thus, the particles are bound to their mean position on time scales smaller than some characteristic

Table 1. The best-fit parameters for the Bellour *et al.* [36] model for the $\langle \Delta r^2(t) \rangle$ curves of microspheres moving in Brownian motion in different fd virus suspensions. ($T = 25\,^\circ$C, $a = 1\,\mu$m, and $\varphi = 0.03$), as well as measured l^* values for each suspension.

c (mg/ml)	[NaCl] (mM)	$6\delta^2$ (nm^2)	D_m (m^2/s) $\times 10^{16}$	D_0 (m^2/s) $\times 10^{13}$	α	l^* (μm)
15.3	100	149.75	2.3567	0.3455	0.28	174.2
15.3	225	188.76	3.8593	0.2738	0.34	158.8
20.1	103	152.22	1.6353	0.5632	0.23	153.9
20.0	228	272.42	1.7950	0.4241	0.24	169.8
20.0	303	277.91	1.4753	0.2012	0.26	127.2
24.3	227	73.50	0.6351	0.1903	0.25	125.1
24.9	300	170.70	3.1125	0.6434	0.25	175.5
24.9	402	196.32	1.1644	0.7311	0.20	156.5
50	225	84.06	2.2204	0.6010	0.25	143.5

time. At long times, the motion again becomes diffusive, $\langle \Delta r^2(t) \rangle = 6D_m t$, where D_m is the diffusion coefficient for the particles at long times. Therefore, it was proposed that $\langle \Delta r^2(t) \rangle = 6\delta^2(1 - e^{-(\frac{D_0}{\delta^2}t)})(1 + \frac{D_m}{\delta^2}t)$ to have the prescribed diffusion motion at long times. However, this expression did not describe correctly the dynamics at the plateau onset time, because dynamics of the particles exhibits a broad time relaxation spectrum. This led to include the parameter α, as shown in eq. (4); $\alpha = 1$ indicates monoexponential relaxation, and the smaller α the larger relaxation spectrum. Thus, according to this model, there are three different regimes for the particle motion: a) at short times, the particles with a Brownian dynamics diffuse freely in the fluid where the supramolecular structures are embedded with a diffusion coefficient D_0; b) at intermediate times, the MSD remains constant for a given time interval; here particles are in Brownian motion trapped in a cage, and c) at longer times, the motion again becomes diffusive. To obtain the real and complex components of $G^*(\omega)$, the method of applying directly a Laplace transform on the fitting curve to $\langle \Delta r^2(t) \rangle$, using analytical continuity ($s \to i\omega$), and eq. (2) to get eq. (3) may be very accurate inside the frequency extremes of the data, but introduces errors near the frequency extremes due to data truncation. Therefore, other method was used based on Mason's logarithmic derivative method [33,38], where $\langle \Delta r^2(t) \rangle$ is expanded locally around the frequency of interest using a power law and retaining the leading term. Thus, the viscoelastic modulus can be calculated through

$$G'(\omega) = |G^*(\omega)| \cos(\pi\alpha(\omega)/2) \quad \text{and}$$
$$G''(\omega) = |G^*(\omega)| \sin(\pi\alpha(\omega)/2), \quad (5)$$

where $|G^*(\omega)| \approx \frac{k_B T}{\pi a \langle \Delta r^2(1/\omega) \rangle \Gamma[1+\alpha(\omega)]}$, Γ is the gamma function, and

$$\alpha(\omega) \equiv \frac{\mathrm{d}\ln\langle \Delta r^2(t) \rangle}{\mathrm{d}\ln t}\bigg|_{t=1/\omega}.$$

The evaluation of α is made on the fitting curve to $\langle \Delta r^2(t) \rangle$, eq. (4). According to (5), it is important to note that the obtained range in the $G'(\omega)$ and $G''(\omega)$ curves

would be determined by the inverse time values of the range where the MSD could be measured. In a few cases, as mentioned above, Laplace transform of the fitting curve, eq. (4), was also employed to extend slightly the MSD at long times, with the aim of extending slightly G' and G'' at lower frequencies (using eq. (2) to get eq. (3)) to observe with better detail the crossing between the G' and G'' curves. In these cases, the fitting procedure extended the frequency range for the elastic and viscous modulus from 5 to 2 rad/s. Here, just the curves that completely overlapped were used.

Finally, l^* was obtained from transmittance and reflectance measurements of the samples to be investigated, using an integrating sphere. This method is described elsewhere [39]. Just to assess the quality of our l^* measurements in colloidal suspensions of particles with different sizes and particle volume fractions, we calculated l^* using Mie scattering theory following the procedures developed by several authors [40–42]. The agreement between l^* values measured with the method employing an integrating sphere and l^* values calculated with Mie scattering theory was excellent. There is just a 3.8% mean deviation between theory and experiment. Other tests can be found elsewhere [39] l^* values for some of the virus suspensions studied here are presented in table 1; $L/l^* \sim 15$.

It is not easy to determine the error bars in DWS. Using wormlike micellar systems where defined quantities can be measured, it is usual for a sample measured in different days to have an error bar of $\sim 7\%$ in the determination of modulus and of $\sim 8\%$ in the relaxation time [37]. So, we assign an error bar in our measurements of 7–8%.

3 Results and discussion

Bacteriophage fd prepared as mentioned in the Experimental section was suspended and diluted for its observation and assessment of purity and integrity with TEM and AFM. Figure 1 presents different images of fd virus at different amplifications obtained when a drop of a dilute suspension was deposited on freshly cleaved mica. Here, we observe their rugged surface and both virus ends that are not of the same size. Although we were not able to resolve
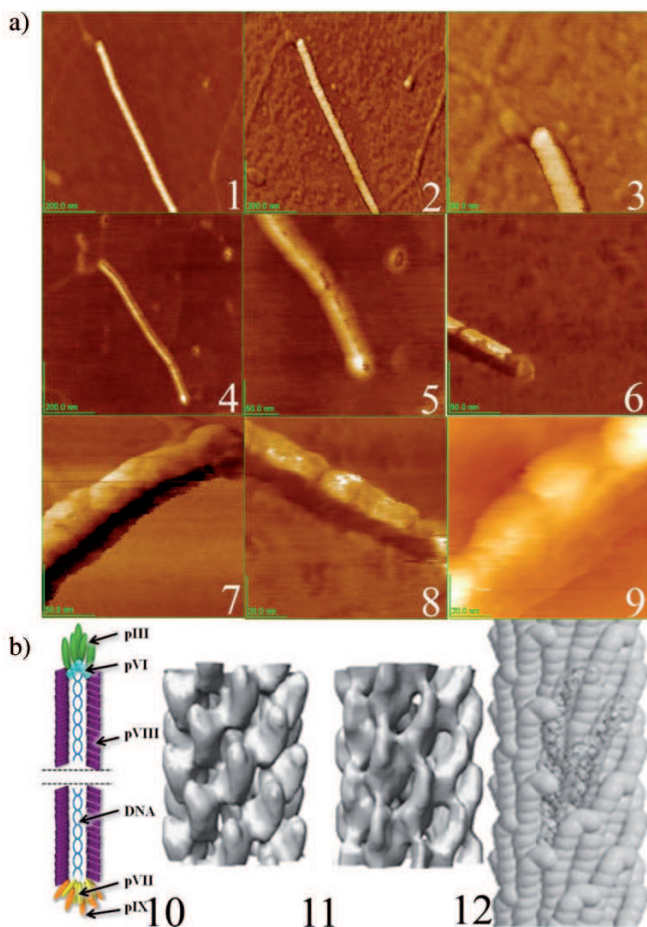
Fig. 1. a) AFM images of fd virus. 1) topography 800×800 nm; 2) phase lag of 1) 800×800 nm; 3) phase lag 300×300 nm; 4) topography 800 × 800 nm; 5) topography 600 × 600 nm; 6) phase lag 200 × 200 nm; 7) phase lag 200 × 200 nm; 8) topography 100 × 100 nm; 9) phase lag 100 × 100 nm. b) Current models to explain the capside of the virus: 10) schematics of the fd virus structure. 11) Model using image reconstruction by cryo-electron microscopy [43] 12) model derived by X-ray fibre diffraction and solid state NMR data [5].

Fig. 2. Images of the bacteriophage fd network obtained with: A) TEM and B) AFM. Inset in (A) presents a dilute virus sample.

Fig. 3. c *vs.* [NaCl] diagram with the location of the different phases of the bacteriophage fd suspension and the phase separation lines (dotted lines are guides to the eye) as given in refs. [44] and [45]. In this diagram, the concentrations of the suspensions studied in the present work are marked with big diamonds.

the protein ultra structure, images at very high resolution were obtained. For a comparison, we included in fig. 1 a schematic diagram of the virus showing its DNA and capside formed with its minor coat proteins (pIII, pVI, pVIII, and pIX) and its major coat ones (pVIII), a model image reconstruction obtained by cryo-electron microscopy [43], and a model derived by X-ray fibre diffraction and solid state NMR data [5]. A more detailed image of the kind of network we are dealing with in a bacteriophage suspension is presented in fig. 2a, where microspheres will be embedded to perform the DWS experiments. Here, a drop of fd virus suspension was deposited on a copper TEM grid and on freshly cleaved mica; the virus network is easily observed by TEM and AFM, respectively. In fig. 3, we present a c *vs.* [NaCl] diagram with the location of different phases of the bacteriophage suspension [44,45], where

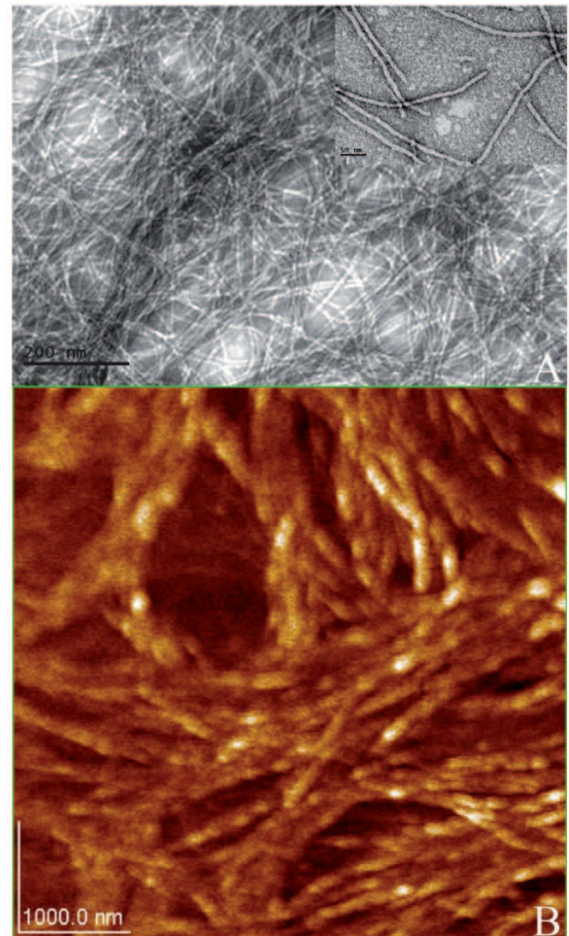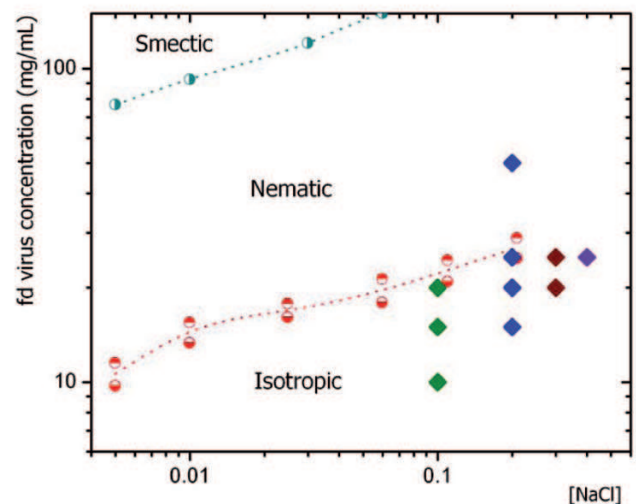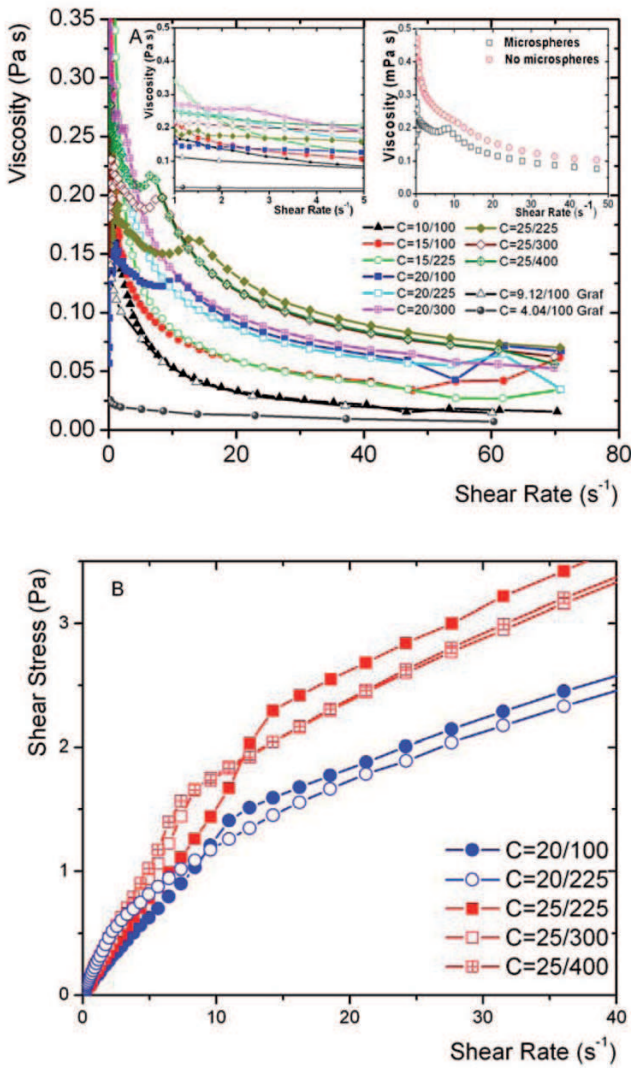**Fig. 4.** a) η *vs.* $\dot{\gamma}$ at different virus and salt concentrations. Left inset: same as in main figure, but at low values of $\dot{\gamma}$. Right inset: η *vs.* $\dot{\gamma}$ curves for a suspension in the nematic phase presenting a peak, and for the same suspension, but with embedded microspheres ($a = 1\,\mu$m, $\varphi = 0.03$). b) σ *vs.* $\dot{\gamma}$ for suspensions presenting a maximum in the viscosity curve of the main figure. Notation: fractions correspond to virus concentration/salt concentration.

we have marked the concentration location of the suspensions studied in the present work, namely, at 25, 20, and 15 mg/mL. For the first two suspensions, we studied three salt concentrations and for the latter, just two salt concentrations. We have two additional studied suspensions in the diagram, one at $c = 10$ mg/mL to compare with data in the literature, and another in the nematic phase (50 mg/mL) that will be discussed later.

3.1 Mechanical rheology

Figure 4a presents the viscosity *vs.* shear rate obtained with a cone-plane cell, for different virus and salt concentrations. Here, we included for comparison data from Graf

et al. [19], for the case of $c = 4.04$ and 9.12 mg/mL, both at [NaCl] = 100 mM. The latter data are close to our measurements at 10 mg/mL, which shear thins as $\dot{\gamma}$ increases. However, at lower shear rates, our measured viscosities are slightly larger. This might be due to the fact that our suspension is slightly more concentrated. At $c = 15$ mg/mL, suspensions shear thin as $\dot{\gamma}$ increases, and the viscosity values are not so different when the salt concentration is varied from [NaCl] = 100 to 225 mM. The case of $c = 20$ mg/mL and [NaCl] = 100 mM presents a peak at $\dot{\gamma} \sim 11.2\,$s^{-1}. After that peak, the suspension shears thins in the same way as in [NaCl] = 225 and 300 mM. For the case of $c = 25$ mg/mL, all the suspensions present a peak no matter the salt concentration, [NaCl] = 225, 300, and 400 mM. As in the previous examples, after the peak they shear thin following the same trend and viscosity values are close. The $\dot{\gamma}$ values where the maxima of the peaks are found in these suspensions decrease as the salt concentration increases, $\dot{\gamma} \sim 13.3$, 8, and $6.7\,$s^{-1} for [NaCl] = 225, 300, and 400 mM, respectively. In all the cases at low shear rates ($\dot{\gamma} \sim 1\,$s^{-1}) before the peak, the suspensions with more added salt present slightly larger viscosities (see left inset of fig. 4a). At these high ionic strengths, the virus charge is surely more efficiently screened making them less rigid and consequently less prone to be aligned by one side, and by the other the excluded volume is smaller; then, suspensions are slightly more viscous and larger shear rates are needed to align the viruses. However, the most important feature in these curves is the viscosity peak at a specific $\dot{\gamma}$. There are a few reports showing this feature in η *vs.* $\dot{\gamma}$ curves, all coming from the same group [13,15,16]. These authors studied suspensions at several virus concentrations up to 23.7 mg/mL, with [NaCl] = 100 mM; here, dextran was added to widen the biphasic region [13,15]. In particular, the observed peaks [16] occur at large values of $\dot{\gamma}$, when no salt and dextran is added, consistent with the trend we found. The larger salt concentration corresponds to the lower $\dot{\gamma}$ where peaks are found. Taking into account that our samples are located at the borderline of the nematic-isotropic phase transition, and that the bimodal will be modified by flow, those peaks must correspond to a transition from tumbling to wagging flow as in [16] where, as in our case, the biphasic region in the $\dot{\gamma}$ *vs.* c diagram is not wide. The two regions of shear thinning separated by a peak in the viscosity *vs.* $\dot{\gamma}$ indicate that at that shear rate the ordering in the system is partly lost, contrary to what is expected when the degree of alignment increases with the shear rate. For different shear rate and fd concentrations, viscosity response of fd suspensions to flow reversals has revealed three characteristic regions [13,16] one where viscosity shows strongly damped oscillations, a region where viscosity is weakly damped (here viscosity reaches its local maximum), and finally a region where the viscosity response is very strongly damped. The damping constant and the tumbling period show a sharp increase at the viscosity peak. This kind of behavior has been predicted earlier [46,13], where it was argued that the nematic phase will tumble due to the torque that is exerted on those rods which have an orientation in the wings of

the orientational distribution function. This torque is then transmitted to the rest of the distribution due to strong excluded-volume interactions between the rods. Nevertheless, during the tumbling process the distribution passes the angle corresponding to the extensional direction of the velocity gradient tensor in shearing flow. At this point the orientational distribution of the rods will be distorted with the result that the ordering will be partly lost. With increasing shear rate this effect becomes stronger and as a consequence the experimentally observed viscosity will increase. At a critical shear rate this effect is so strong that the ordering is completely lost. Since isotropically distributed rods flow align, the director will not pass the angle of extensional flow and return to the flow direction. This is the point where the wagging regime comes into play and the viscosity reaches a maximum. The damping of oscillations in the tumbling regime is probably caused by an interaction between different nematic domains, and the explanation of the transition from strongly damped to weakly damped is that in the wagging state the director oscillates around the flow direction. Compared to the tumbling state, the wagging state corresponds to a more ordered state where the polydomain structure disappears, as was observed when the viscosity reached a peak [13]. This behavior also was found in the theoretical predictions of the Doi-Edwards-Hess theory of the nematic director angle, the magnitude of nematic order parameter, and the average stress as a function of strain after a start up of the flow for fd suspensions [16]; here the flow behavior can exhibit a sharp transition from the tumbling behavior, where the director continuously rotates, to the wagging behavior where the director hops back and forth between two well-defined angles. At higher shear rates the director is found to be flow aligning as it was found in the experiments.

In the right inset of fig. 4a, we present two η *vs.* $\dot{\gamma}$ curves, one for a suspension in the nematic phase ($c = 50 \, \text{mg/mL}$, [NaCl] $= 225 \, \text{mM}$), which presents a peak, and another for the same suspension, but with embedded microspheres (particle radius $a = 1 \, \mu\text{m}$, at $\varphi = 0.03$), where the peak due to the tumbling-to-wagging transition is absent. The average distance between the colloidal particles surfaces is approximately equal to $3L_c$, at $\varphi = 0.03$. Apparently microspheres destroy the nematic order, because the system is behaving as if it was in a paranematic state. Figure 4b presents flow curves, σ *vs.* $\dot{\gamma}$, for suspensions presenting a peak in the viscosity curve. Here, shear thickening is clearly observed at $\dot{\gamma}$ values where the peaks are found.

Figure 5 presents typical elastic and viscous moduli in a frequency range of $0.1 \leq \omega \leq 30 \, \text{rad/s}$ of virus suspensions, at $c = 25 \, \text{mg/ml}$ and different salt concentrations, measured by mechanical rheometry. For other concentrations, the results are quite similar. $G''(\omega) \geq G'(\omega)$ for all frequencies below a crossover frequency located around $\omega_c \sim 20 \, \text{rad/s}$. Therefore, fd virus suspensions exhibit a liquid-like behavior along this frequency range. At frequencies above this crossover frequency, there is a plateau-like region, as was observed by Schmidt *et al.* [17] at lower virus and salt concentrations. At frequencies above
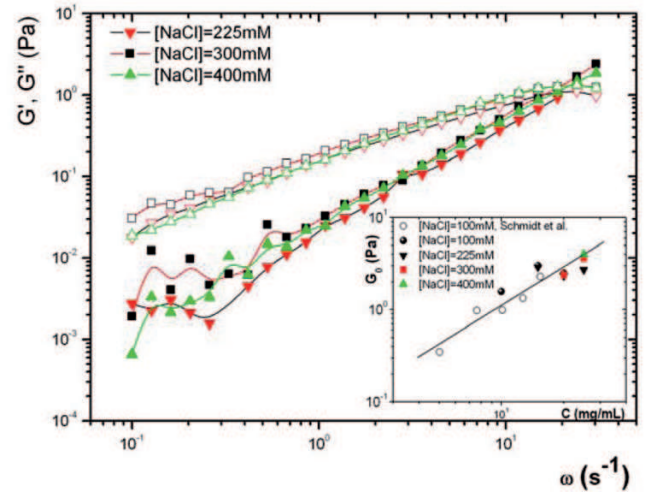

Fig. 5. Elastic (filled symbols) and viscous (open symbols) moduli in a frequency range $0.1 \leq \omega \leq 30 \, \text{rad/s}$ for fd virus suspensions at $c = 25 \, \text{mg/mL}$, and different salt concentrations measured with mechanical rheometry. Lines are guides to the eye. Inset: concentration dependence of G_0 obtained combining our mechanical results and those of Schmidt *et al.* [17].
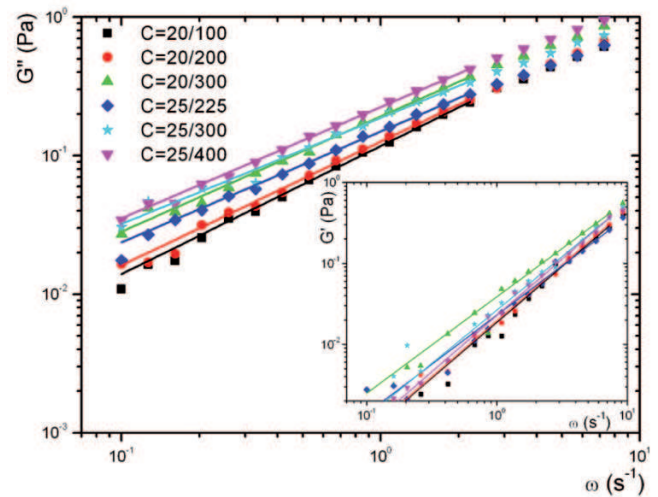

Fig. 6. Below the crossover frequency $\omega_c \sim 20 \, \text{rad/s}$, the frequency dependence of the viscoelastic moduli follows approximately a power law. $G'(\omega) \sim \omega^{1.1-1.3}$ and $G''(\omega) \sim \omega^{0.7-0.9}$. Notation: fractions correspond to virus concentration/salt concentration.

$40 \, \text{rad/s}$, the inertia of the employed rheometric cell geometry becomes important and the results are not entirely reliable. Salt concentration does not modify the $G'(\omega)$ and $G''(\omega)$ curves in an important way; the measurements are quite close. Since we measured suspensions at higher concentrations, the dependence of the plateau modulus, G_0, with concentration can be obtained more precisely, extending the data given by Schmidt *et al.* [17] with our data, as is presented in the inset of fig. 5. G_0 was determined from the relative minima in the phase lag between σ and $\dot{\gamma}$. From these data it follows that $G_0 \sim c$ [1,4]. Below the crossover frequency ω_c, the frequency depen-

dence of the viscoelastic moduli follows approximately a power law, $G'(\omega) \sim \omega^{1.1\text{-}1.3}$ and $G''(\omega) \sim \omega^{0.7\text{-}0.9}$ (see fig. 6). Schmidt *et al.* [17] found essentially the same scaling laws, $G'(\omega) \sim \omega^{0.9\text{-}1.2}$ and $G''(\omega) \sim \omega^{0.7\text{-}0.9}$ at these frequencies. At low frequencies ($\omega \leq 0.5\,\text{rad/s}$), our $G'(\omega)$ measurements are noisy, probably due to the small value of the modulus there. Below ω_c, the moduli increase as c increases; for a fixed value of c, the larger the salt concentration the larger the $G''(\omega)$. This tendency is not so clear in $G'(\omega)$, since values are similar within the experimental error.

3.2 DWS microrheology

Figure 7a presents a typical $\langle \Delta r^2(t) \rangle$ *vs. t* curve measured for microspheres ($a = 1\,\mu\text{m}$) dispersed in a virus suspension, which spans over seven orders of magnitude in time. In this particular case $c = 24.9\,\text{mg/mL}$, $[\text{NaCl}] = 300\,\text{mM}$, and $T = 25\,^\circ\text{C}$. The $\langle \Delta r^2(t) \rangle$ curve is the result of numerical inversion of eq. (1), where $g^{(2)}(t)$ came from a DWS experiment (see inset in fig. 7a). Afterwards, the $\langle \Delta r^2(t) \rangle$ was fitted to the model given by Bellour *et al.* [36], as described in the experimental section. It is important to note that no microsphere flocculation was observed during the experiments. l^* was measured after sample preparation and after DWS measurement; l^* gave the same results within the experimental error. If some flocculation occurred, it would be detected, because l^* measurements are sensitive to clustering. In addition, after DWS experiments, a sample drop was observed by optical microscopy and no aggregation was detected, see fig. 7b. In fig. 7a, we observe three different regimes of motion. At short times, there is a regime where $\langle \Delta r^2(t) \rangle$ is almost a linear function of time; $\langle \Delta r^2(t) \rangle = 6D_0 t$, where D_0 is the local diffusion coefficient in the solvent at infinite dilution. At intermediate times, $\langle \Delta r^2(t) \rangle$ presents a shoulder revealing that microspheres are not trapped by the fd virus network or they can leave it easily. At longer times, $\langle \Delta r^2(t) \rangle$ is again a linear function of time, $\langle \Delta r^2(t) \rangle = 6D_m t$, where D_m is the diffusion coefficient in the suspension at long times. It is interesting to note the clear difference between the $\langle \Delta r^2(t) \rangle$ curves for suspension of fd virus and the same curves for another suspension with threadlike structures, the worm-like micellar solution [26,36,37]. For comparison, in fig. 7a a typical $\langle \Delta r^2(t) \rangle$ curve for a wormlike micellar network was included that is made of N-tetradecyl-N,N-dimethyl-3-ammonio-1-propanesulfonate (TDPS), sodium dodecyl sulfate (SDS), and salty water [36]. Here, the network is made by wormlike micelles that undergo an equilibrated process of breaking and recombination trapping more efficiently the particles, but allowing them to escape after some time [26,36,37]. Instead the fd suspension $\langle \Delta r^2(t) \rangle$ presents just an inflection point around $1\,\text{ms}$. All the $\langle \Delta r^2(t) \rangle$ curves for the fd suspensions share this behavior. As a consequence of this difference, as we will see in the $G'(\omega)$, virus suspensions do not present a region with a constant plateau modulus.

Several $\langle \Delta r^2(t) \rangle$ curves for microspheres ($a = 1\,\mu\text{m}$) moving in Brownian motion in different virus suspensions
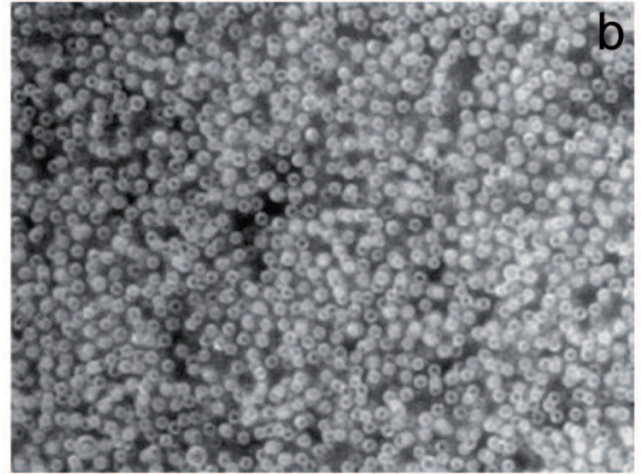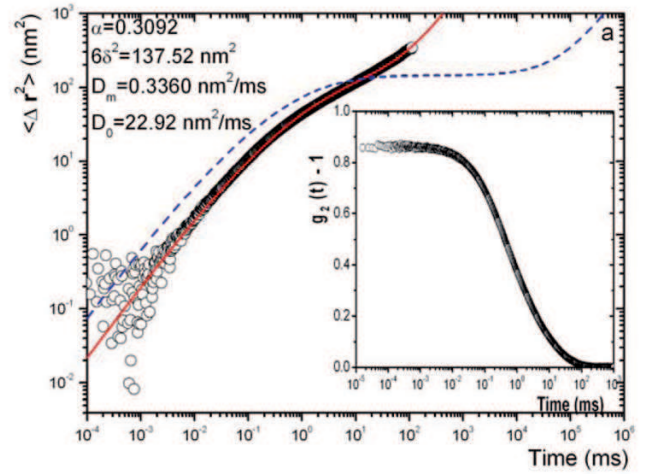

Fig. 7. (Colour on-line) a) Typical $\langle \Delta r^2(t) \rangle$ curve measured for microspheres ($a = 1\,\mu\text{m}$) dispersed in a virus suspension ($c = 24.9\,\text{mg/mL}$, $[\text{NaCl}] = 300\,\text{mM}$, and $T = 25\,^\circ\text{C}$). Red line, best fitting to the Bellour *et al.* model [36]. Dashed line corresponds to a typical $\langle \Delta r^2(t) \rangle$ curve for a wormlike micellar network (TDPS/SDS/brine, $[\text{NaCl}] = 0.22$, microspheres of $a = 1\,\mu\text{m}$ and $\varphi = 0.03$; details in ref. [37]). Inset: field autocorrelation function that produced the $\langle \Delta r^2(t) \rangle$ through numerical inversion. b) Typical optical microscopy image of a drop of sample of a fd suspension ($c = 20\,\text{mg/mL}$, $[\text{NaCl}] = 228\,\text{mM}$) embedded with microspheres ($a = 1\,\mu\text{m}$) between a slide and a cover slide after a DWS experiment, where several layers can be observed; no microsphere aggregation can be observed.

are presented in fig. 8, at $25\,^\circ\text{C}$. The best-fit parameters for the Bellour *et al.* [36] model for those curves, *i.e.*, D_0, δ, α, and D_m, are shown in table 1. For a given fd concentration, the $\langle \Delta r^2(t) \rangle$ curves are relatively close, and salt addition sometimes increases the MSD. For a given salt concentration, the $\langle \Delta r^2(t) \rangle$ values are lower as the virus concentration increases (lower panel fig. 8). The microsphere diffusion at short times, D_0, must correspond to diffusion of microspheres in salty water. Here, in our case, the microspheres are not at infinite dilution and surely particles do not diffuse freely due to electrostatic interaction. To obtain the D_0 values, it is not practical to make an
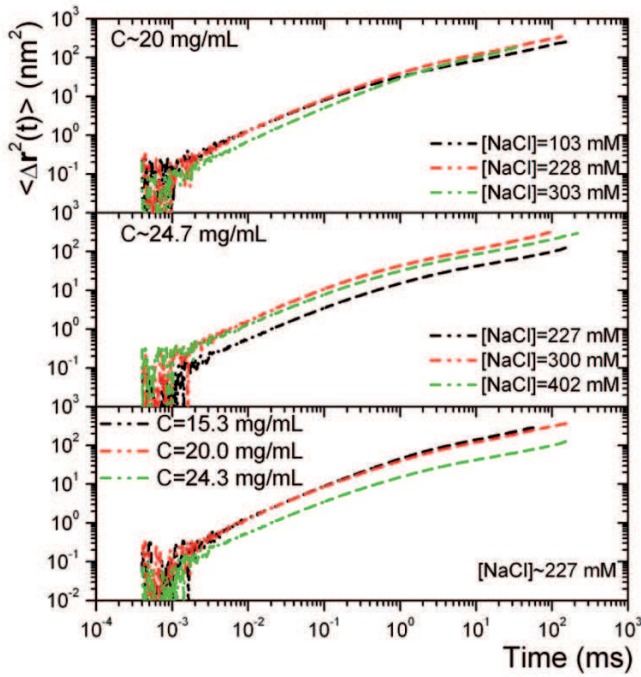
Fig. 8. $\langle \Delta r^2(t) \rangle$ *vs.* t for microspheres ($a = 1\,\mu$m) moving in Brownian motion in different fd suspensions at $25\,^\circ$C. In the two upper panels, c is a constant, and the salt concentration is varied ("$\sim$" is used to remark that those values are averages of samples of table 1, with slightly different concentration). In the lower panel, the salt concentration is fixed and c is varied.

independent measurement of D_0 for microspheres in salty water, because particle flocculation cannot be avoided; the quantity of added salt in the suspensions is important. Therefore, these numbers were obtained as fitting parameters of the model. As expected, the D_0 values obtained through the fittings are relatively close, but smaller than the diffusion coefficient of these microspheres in plain water at infinite dilution and at $T = 25\,^\circ$C ($D \sim 2.29 \times 10^{-13}\,\text{m}^2/\text{s}$). $6\delta^2$ gives an estimation of the mean square displacement of the microspheres in a cage that in this case is almost nonexistent, since microspheres can easily leave it. The trend followed by $6\delta^2$ is not clear because ionic interaction is playing an important role. At the same salt concentration there is a maximum in $6\delta^2$ between $c = 15$ and $c = 25\,\text{mg/mL}$, however, $6\delta^2$ increases with salt addition. This seems to indicate that at high salt concentrations, electrostatic interactions screen the fd virus charge, and the virus becomes more flexible and thinner for the microspheres. Therefore, microspheres feel the network not so compact, as if they would have more room to move and therefore with less opportunity to be trapped. The diffusion coefficient for long times D_m is at some degree dominated by the long-time viscosity of the suspension η_m through $D_m = k_B T/6\pi a\eta_m$. As viscosity increases, by increasing the concentration of the bacteriophages, D_m decreases. This is easily observed in table 1, when salt concentration is constant. However, ionic interaction plays an important role because at constant c, the viscosity slightly increases with salt addition as noted

above, but as observed in table 1, D_m does decrease as salt is added. The dynamics of the microspheres at the plateau onset time shows a broad relaxation spectrum, revealed by the values for the α parameter. The average value for α in the fd suspensions presented in table 1 is $\alpha = 0.26$. The smaller α, the larger the relaxation spectra ($\alpha = 1$ indicates monoexponential relaxation). This value is relatively similar to the case when wormlike micelles are the thread-like structures embedded in the fluid; for CTAB/NaSal ($\alpha \sim 0.23$–0.26) [26], CTAC$_7$SO$_3$ ($\alpha = 0.25$–0.30) [36], and of TDPS/SDS (0.18–0.28) [37]. The virus suspension corresponding to $c = 50\,\text{mg/mL}$ and $[\text{NaCl}] = 225\,\text{mM}$ was measured in the nematic phase, despite it is not an isotropic media and the current form of DWS theory cannot be used. However, the inclusion of the microspheres to use DWS apparently destroyed the nematic order, as shown in the top right inset of fig. 4a, where the tumbling-wagging transition peak is absent. In the same way, l^* measured for this sample produced a value similar to the Mie scattering theory calculation in anisotropic media, consistent with a lack of nematic ordering. Then, this apparently is a way to explore denser suspensions than those permitted by phase equilibrium and to be consistent with DWS theory. The shapes of $\langle \Delta r^2(t) \rangle$ are very similar to the measurements in the isotropic phase. However there is a change of tendency in $6\delta^2$ and of D_m as observed in table 1. In this particular case, the cage is abnormally small and D_m is larger than expected.

In a previous report, Kang *et al.* [47] measured the short- and the long-time diffusion for particles with different radius ($a = 3, 35, 210,$ and $500\,\text{nm}$) in dilute fd suspensions, up to $\sim 1\,\text{mg/ml}$, at two values of the ionic strength (10 and $110\,\text{mM}$) using a combination of fluorescence correlation spectroscopy, DLS, and video microscopy. Here, these authors also evaluated the MSD for these particles in short periods of time ~ 0–$5\,$s depending on the size of the particles. It is difficult to compare their results and our results, because in our case we use much larger particles ($a = 1\,\mu$m) embedded in highly concentrated suspensions (~ 15.3–$50\,\text{mg/ml}$). However, several trends in our measurements are similar to their results for big microspheres ($500\,\text{nm}$); diffusion coefficients decreases when fd concentration increases, and the ratios for D_m/D_0 are small (in our case averaging over all the studied concentrations $D_m/D_0 \sim 0.005$ and in their study $D_m/D_0 \sim 0.08$ at $1\,\text{mg/ml}$). For the same reasons, the MSDs are orders of magnitude smaller than in Kang *et al.* [47].

Figure 9 presents both $G'(\omega)$ and $G''(\omega)$ as a function of the angular frequency ($2 \leq \omega \leq 10^6$) obtained from the MSDs for several bacteriophage suspensions. Two crossings between $G'(\omega)$ and $G''(\omega)$, as well as a plateaulike region are clearly observed. When $G'(\omega)$ and $G''(\omega)$ are obtained evaluating the power spectral density of the thermal fluctuations of embedded micron-sized particles [20], those features cannot be observed well because of the accumulated error, and of the finite high-frequency cut-off of the Kramer-Kronig (KK) integral relation to obtain $G'(\omega)$. In general, the suspension is mainly viscous, $G''(\omega) > G'(\omega)$, except in the plateaulike region. This is probably due to the virus semiflexiblibility ($L_c \sim l_p$), and
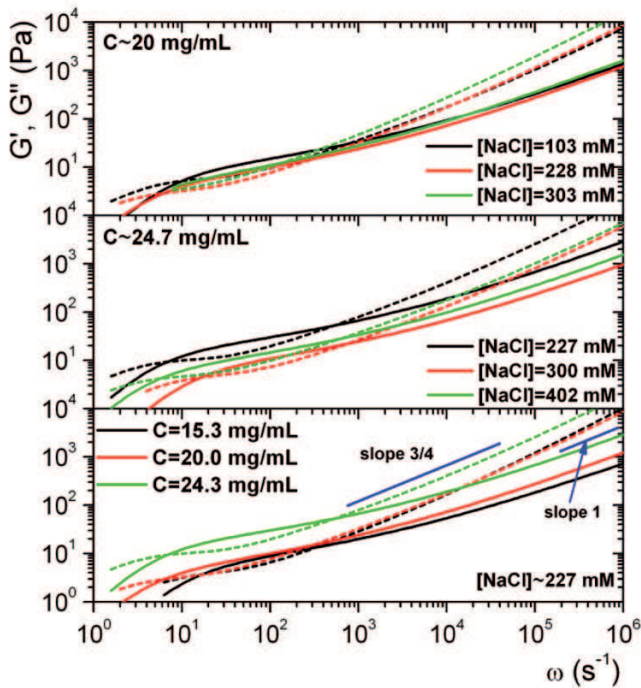
Fig. 9. $G'(\omega)$ (continuous line) and $G''(\omega)$ (dashed lines) as a function of the angular frequency for several fd suspensions. In the two upper panels, c is a constant, and the salt concentration is varied ("$\sim$" is used to remark that those values are averages of samples of table 1, with slightly different concentration). In the lower panel, the salt concentration is fixed and c is varied.

Fig. 10. A comparison of $G'(\omega)$ (full circles) and $G''(\omega)$ (open circles) measured with DWS and through evaluating the power spectral density of the thermal fluctuations of embedded micron-sized particles carried out by Addas *et al.* [20] Insets: a) comparisons between DWS results and mechanical rheometry developed by Schmidt *et al.* [17] and b) by this work (lower inset).

that its surface is negatively charged preventing any kind of sticking among them. At $c = 20\,\mathrm{mg/mL}$, $G'(\omega)$ apparently does not depend on the salt concentration, and for $c = 24.7\,\mathrm{mg/mL}$ the trend is not clear because the results for the case of $402\,\mathrm{mM}$ and $300\,\mathrm{mM}$ are within the experimental error; although, $G'(\omega)$ is larger for $227\,\mathrm{mM}$. For $G''(\omega)$ the trend with salt concentration is unclear. For a specified salt concentration ($227\,\mathrm{mM}$), the larger $G'(\omega)$ is presented by the suspension more concentrated in the bacteriophage. $G''(\omega)$ apparently follows the same trend, although the values for $c = 15.3$ and $c = 20\,\mathrm{mg/mL}$ have the same values, within the experimental error. In fig. 9, reference lines are included showing that at frequencies around $\sim 10^4\,\mathrm{s}^{-1}$ the viscous modulus exhibits a power law behavior, $G'' \sim \omega^{3/4}$, and at high frequencies where the solvent contribution dominates the modulus follows $G'' \sim \omega^1$.

Figure 10 presents a comparison for the $G'(\omega)$ and $G''(\omega)$ curves obtained with the DWS measurements presented in this work, and with the thermal particle fluctuations method carried out by Addas *et al.* [20], where the power spectral density of the thermal fluctuations of embedded micron-sized particles is evaluated. In this figure, we included a few of their experimental points to make the comparison. With DWS, it is possible to extend the moduli measurements to higher frequencies, and the DWS data is much less noisy than the data obtained by Addas *et al.* [20] (see fig. 10 of ref. [20]). Increas-
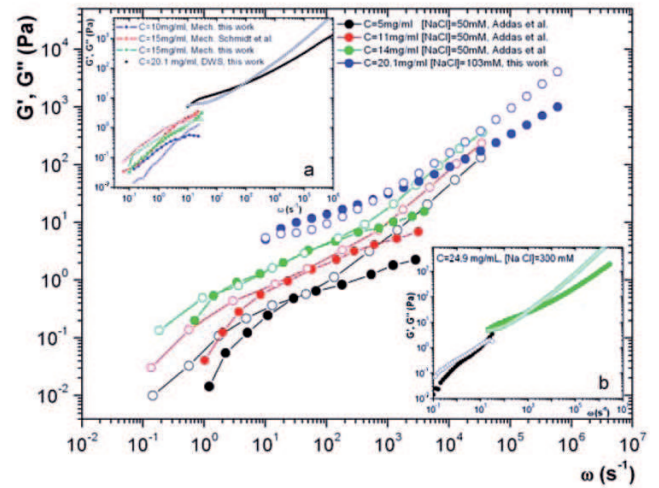
ing the virus concentration, the magnitude of the viscoelastic moduli also increases. Our data follows the same trend found by these authors, despite salt concentration in both studies is different ([NaCl] $= 50\,\mathrm{mM}$ in Addas *et al.* [20] and [NaCl] $= 103\,\mathrm{mM}$ in this work). However, as observed in our study, salt addition does not change the microrheology in an important way (see figs. 8 and 9). We present comparisons between mechanical rheometry and microrheology in fig. 10. In the inset (a) our DWS results are compared with mechanical rheology developed by Schmidt *et al.* [17] and in inset (b) with the mechanical rheology made by us. Of course mechanical rheology can measure only at very low frequencies, and transmission DWS can measure at the intermediate and high frequencies. However, both techniques can measure the first crossing of $G'(\omega)$ and $G''(\omega)$ that increases with fd concentration. From this comparison it is clear that the frequency of the first crossing is well reproduced by DWS, however, DWS always presents the crossing at slightly higher moduli values.

As mentioned in the Introduction, Morse proposed a model for describing the linear rheological properties of tightly entangled isotropic solutions of semiflexible polymers using a tube model [18,23,24]. In this model, the high-frequency regime is dominated by a large tension contribution yielding a complex modulus that varies as $G^*(\omega) \sim \omega^\alpha$. The input parameters in the Morse model for a monodisperse polymer solution are: filament density ρ, hydrodynamic filament radius d, solvent viscosity η_s, as well as L_c, l_p, and l_e. d can be estimated ($\sim 10\,\mathrm{nm}$) from the size of the virus, and the only unknown quantity is l_e. Basically, in the framework of this theory, two different methods have been used to estimate this length,
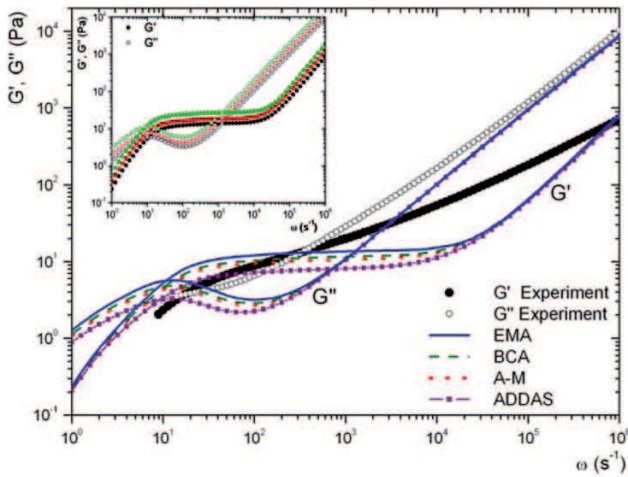
Fig. 11. (Colour on-line) A comparison of the viscoelastic moduli obtained experimentally with DWS and obtained by the Morse model for semiflexible polymers. $\rho = 585.6\,\mu\mathrm{m}^{-2}$ ($c = 15\,\mathrm{mg/mL}$), $d = 10\,\mathrm{nm}$, $\eta_s = 1\,\mathrm{mPa\,s}$, $L_c = 900\,\mathrm{nm}$, $l_p = 2.2\,\mu\mathrm{m}$, and $T = 25\,\mathrm{C}$. $l_e^{\mathrm{Addas}} = 0.49\,\mu\mathrm{m}$, $l_e^{\mathrm{A\text{-}M}} = 0.35\,\mu\mathrm{m}$, $l_e^{\mathrm{BCA}} = 0.32\,\mu\mathrm{m}$, and $l_e^{\mathrm{EMA}} = 0.26\,\mu\mathrm{m}$. Inset: prediction of the Morse model for $c = 15$ (black circles), 20 (red squares), 25 (green triangles) mg/mL, using L_e^{EMA}.

both giving a different power law dependence on ρ and l_p. In one method, the interaction of a polymer chain with just a single nearby polymer chain is considered; therefore, the collective elastic relaxation of the network is neglected. This is the binary collision approach (BCA) producing the expression $l_e^{\mathrm{BCA}} = 3.45\rho^{-2/5}l_p^{1/5}$ (eq. (47) in ref. [24]). The other method treats the surrounding network around a polymer chain as an elastic continuum represented with a shear modulus equal to the self-consistently determined plateau modulus of the solution. This procedure is called the effective medium approach (EMA), which leads to the formula $l_e^{\mathrm{EMA}} = 1.70\rho^{-1/3}l_p^{1/3}$ (eqs. (9) and (65), in ref. [24]). In addition, Addas *et al.* [20] used other two formulae to evaluate l_e. In the first one, they used a combination of the methods just described; here $l_e^{\mathrm{A\text{-}M}} = ((l_e^{\mathrm{BCA}})^4 + (l_e^{\mathrm{EMA}})^4)^{1/4}$ as suggested by Morse to these authors [20]. In the second formula, they considered that the pre-factor b, in the equation $L_e^{\mathrm{Addas}} = b\rho^{-2/5}l_p^{1/5}$, is a universal parameter independent of the kind of polymer system under study. They assigned to this parameter the value $b = 5.4$ based on the rheological results in suspensions of F-actine; Thus, $l_e^{\mathrm{Addas}} = 5.4\rho^{-2/5}l_p^{1/5}$ [20]. Figure 11 presents a comparison between the viscoelastic moduli obtained by DWS experiments and the Morse model for semiflexible polymers. The specific parameters used in these calculations were the following: $\rho = 585.6\,\mu\mathrm{m}^{-2}$ ($c = 15\,\mathrm{mg/mL}$), $d = 10\,\mathrm{nm}$, $\eta_s = 1\,\mathrm{mPa\,s}$, $L_c = 900\,\mathrm{nm}$, $l_p = 2.2\,\mu\mathrm{m}$, and $T = 25\,^{\circ}\mathrm{C}$. For the entanglement length we used $l_e^{\mathrm{Addas}} = 0.49\,\mu\mathrm{m}$, $l_e^{\mathrm{A\text{-}M}} = 0.35\,\mu\mathrm{m}$, $l_e^{\mathrm{BCA}} = 0.32\,\mu\mathrm{m}$, and $l_e^{\mathrm{EMA}} = 0.26\,\mu\mathrm{m}$. As we can observe in fig. 11, along the frequency range $1 \le \omega \le 10^6$ rad/s, the agreement between experiments and theory is not good, in particular because the experimental data show a no-well-developed plateau as is observed in the model calculations, no matter what version of l_e is used. The minimum in $G''(\omega)$ between the crossings is quite pronounced in the model, as compared with the experiment. In the inset of fig. 11, we present the calculated moduli for fd suspensions using L_e^{EMA} at different concentration values, $c = 15, 20, 25\,\mathrm{mg/mL}$. Clearly, we can observe that the shear moduli increase as c increases, but the shape of the moduli is not the right one. To understand the origin of the mismatch, the internal consistency of the $G'(\omega)$ and $G''(\omega)$ curves was tested through evaluating $G'(\omega)$ from $G''(\omega)$ by using the KK integral relations, which in linear response theory comes from the causality principle

$$G'(\omega) = \frac{2\omega^2}{\pi}P\int_0^{\infty}\frac{G''(\omega')/\omega'}{\omega^2 - \omega'^2}\,d\omega', \qquad (6)$$

where P indicates the principal value. As we can observe in fig. 12a, the $G'(\omega)$ curve obtained through introducing the $G''(\omega)$ curve, coming from the Morse model, into the KK equation (eq. (6)), deviates from the $G'(\omega)$ obtained directly from the Morse model, mainly at high frequencies. On the contrary, our experimental values are consistent with the KK equation, as can be observed in the inset of fig. 12a. Here, the DWS experimental $G'(\omega)$ agrees well with the $G'(\omega)$ calculated with KK equations introducing this time the DWS experimental $G''(\omega)$ curve into eq. (6). The KK calculations were carried out fitting a model curve to the viscous modulus. Afterwards, the elastic modulus was estimated through numerical integration, according to eq. (6). The fitting model curve used for $G''(\omega)$ was

$$G''(\omega) = G_0\frac{\omega^{\alpha}\tau_1}{1 + \omega^{\beta}\tau_2^{\gamma}} + \sum_i A_i\omega^{a_i}. \qquad (7)$$

For the case of the calculation for the Morse model, we use only one power law fitting at high frequencies. For the case of the fd virus experimental data, two power laws were necessary to fit the viscous modulus at high frequencies.

Another difference with theory can be noticed with $|G^*| = \sqrt{G'^2 + G''^2}$ at high frequencies, where a power law behavior is observed, $|G^*| \sim \omega^{\nu}$. We found a change of exponent at some particular ω_0 not observed in the calculations using the Morse model. This behavior has been observed in wormlike micelles [26,37,48], but it has not been reported for fd suspensions. In those systems at high frequencies, where time scales are shorter than those of wormlike micelle breakage time, the Maxwellian stress relaxation processes are essentially frozen, and the micelles can be regarded as semiflexible polymer chains. Stress relaxes via intramicellar processes: First, it is dominated by the Rouse-Zimm modes and then by the internal relaxation of individual Kuhn segments. Therefore, G^* exhibits a power law behavior, $|G^*| \sim \omega^{\nu}$, with the exponent $\nu \sim 5/9$ in the Rouse-Zimm regime, which changes to $\nu \sim 3/4$, where the internal bending modes of Kuhn segments dominate. This change occurs at a critical frequency, ω_0, corresponding to the shortest relaxation time
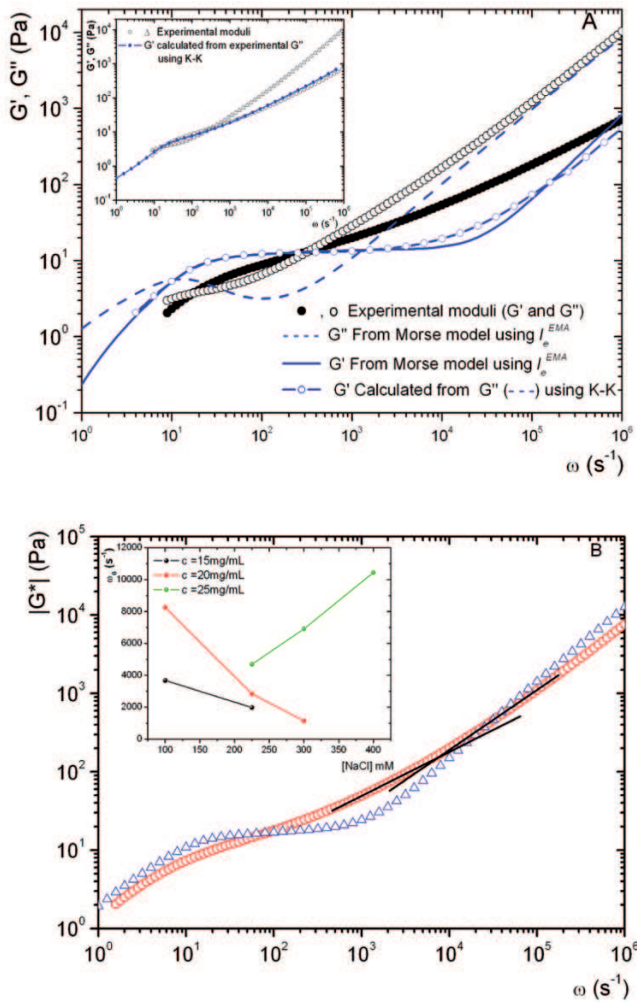
Fig. 12. a) The $G'(\omega)$ curve obtained by introducing the Morse model $G''(\omega)$ curve into the KK equations deviates from the $G'(\omega)$ obtained from the Morse model mainly at high frequencies, $c = 20.1\,\mathrm{mg/mL}$. Inset: the experimental values are consistent with the KK equations, the DWS experimental $G'(\omega)$ agrees well with the $G'(\omega)$ calculated with KK equations introducing this time the DWS experimental $G''(\omega)$ curve into eq. (6). b) Comparison of $|G^*|$ *vs.* ω obtained with DWS microrheology ($\circ$) and with the Morse model ($\triangle$), for a suspension of fd virus with $20.1\,\mathrm{mg/mL}$ and $[\mathrm{NaCl}] = 103\,\mathrm{mM}$, $\omega_0 \sim 8262.6\,\mathrm{s}^{-1}$. The inset presents how ω_0 varies with fd virus and salt concentration.

in the Rouse-Zimm spectrum [48]. We do not know if this mechanism is really operating in fd virus, but in fig. 12 we can observe the power law change. Here, a suspension of $20.1\,\mathrm{mg/mL}$ and $[\mathrm{NaCl}] = 103\,\mathrm{mM}$ presents a $\omega_0 \sim 8262.6\,\mathrm{s}^{-1}$. Intercepts of power laws fittings to $|G^*|$ at high frequencies, with $\nu \sim 3/4$, allowed us to estimate the ω_0 values. In the inset of fig. 12, we present how ω_0 varies with fd and salt concentrations. ω_0 decreases as salt concentration increases for virus concentrations of 15.3 and $20\,\mathrm{mg/ml}$, but on the contrary it increases for the case of $24.3\,\mathrm{mg/ml}$. According to the theory used for wormlike micelles, ω_0 and the persistence length are inversely pro-

portional. However, Morse theory does not involve these quantities, therefore without a proper theory we cannot give a proper explanation for this behavior.

4 Conclusion

Microrheology measurements were performed with a multiple scattering technique (DWS) on bacteriophage fd suspensions in the high concentrated regime, and at different values of ionic strength. We also measured the shear viscosity *vs.* shear rate in these suspensions, and the influence of virus concentration and salt concentration on the shear thinning, and on the peak position of the curves corresponding to a transition from tumbling to wagging flow. This study allowed us to make a comparison between the results of a multiple scattering technique with those obtained with a particle tracking method of embedded particles, where the thermal fluctuations and the power spectral density is used to evaluate the viscoelastic moduli. In general, both methods agree, however the DWS results are much less noisy and can reach larger frequencies. In DWS, the $\langle \Delta r^2(t) \rangle$ of microspheres embedded in the suspensions is first obtained, given an insight of the system through examining the influence of virus concentration and salt concentration on this quantity, over five orders of magnitude in time. From $\langle \Delta r^2(t) \rangle$, the viscoelastic moduli up to high angular frequencies ($10^6\,\mathrm{s}^{-1}$) were calculated.

In addition, a comparison could be made between measured and calculated shear moduli. Calculations were made for a theory for highly entangled isotropic solutions of semiflexible polymers using a tube model developed by Morse, where various ways of calculating the needed parameters were used. Although some features are captured by the model, it is far from the experimental results mainly in the $10\,\mathrm{s}^{-1} < \omega < 10^5\,\mathrm{s}^{-1}$ range. For describing these semiflexible polymer systems, more theoretical work has to be done. In particularly, we found that the theoretical $G'(\omega)$ and $G''(\omega)$ were not consistent with the Kramers Kronig integral relations. On the contrary, the DWS experimental $G'(\omega)$ and $G''(\omega)$ were consistent with them. Other features which are not incorporated in the theory, but that can be clearly observed in the experimental data are: a) $|G^*| \sim \omega^\nu$ also exhibits a change in the power law behavior exponent at high frequencies, from $\nu \sim 5/9$ to $\nu \sim 3/4$, and b) there is an important influence of the ionic force of the media on the microrheology fd suspensions.

References

1. M. Doi, S.F. Edwards, *The Theory of Polymer Dynamics* (Clarendon, Oxford, 1986).
2. L.A. Day, C.J. Marzee, S.A. Reisberg, A. Casadevall, Ann. Rev. Biophys. Biophys. Chem. **17**, 509 (1988).

3. S. Bhattacharjee, M.J. Glucksman, L. Makowsky, Biophys. J. **61**, 725 (1992).
4. A.C. Zeri, M.F. Mesleh, A.A. Nevzorov, S.J. Pella, Proc. Natl. Acad. Sci. U.S.A. **100**, 6458 (2003).
5. D.A. Marvin, L.C. Welsh, M.F. Symmons, W.R.P. Scott, S.K.J. Straus, Mol. Biol. **355**, 294 (2006).
6. S.K. Straus, W.R.P. Scott, M.F. Symmons, D.A. Marvin, Eur. Biophys. J. **37**, 521 (2008).
7. K. Zimmermann, H. Hagedorn, C.Ch. Heuck, M. Hinrichsen, H. Ludwig, J. Biol. Chem. **261**, 1653 (1986).
8. D. Lopez-Diaz, R. Castillo, Soft Matter **7**, 5926 (2011).
9. Z. Dogic, S. Fraden, Phys. Rev. Lett. **78**, 2417 (1997).
10. Z. Dogic, S. Fraden, Langmuir **16**, 7820 (2000).
11. Z. Dogic, S. Fraden, Curr. Opin. Colloid Interface Sci. **11**, 47 (2006).
12. J.K.G. Dhont, M.P. Lettinga, Z. Dogic, T.A.J. Lenstra, H. Wang, S. Rathgeber, P. Carletto, L. Willner, H. Frielinghaus, P. Lindner, Faraday Disc. **123**, 157 (2003).
13. M. Lettinga, J.K.G. Dhont, J. Phys.: Condens. Matter **16**, S3929 (2004).
14. K. Kang, M. Lettinga, Z. Dogic, J.K.G. Dhont, Phys. Rev. E **74**, 26307 (2006).
15. M. Ripoll, P. Holmqvist, R.G. Winkler, G. Gompper, J.K.G. Dhont, M.P. Lettinga, Phys. Rev. Lett. **101**, 168302 (2008).
16. M.P. Lettinga, Z. Dogic, H. Wang, J. Vermant, Langmuir **21**, 8048 (2005).
17. F.G. Schmidt, B. Hinner, E. Sackmann, J.X. Tang, Phys. Rev. E **62**, 5509 (2000).
18. D.C. Morse, Macromolecules **31**, 7044 (1998).
19. C. Graf, H. Kramer, M. Deggelman, M. Hagenbüchle, C. Johner, C. Martin, R. Weber, J. Chem. Phys. **98**, 4920 (1993).
20. K.M. Addas, C.F. Schmidt, J.X. Tang, Phys. Rev. E **70**, 021503 (2004).
21. F. Huang, R. Rotstein, S. Fraden, K.E. Kasza, N.T. Flynn, Soft Matter **5**, 2766 (2009).
22. Z.K. Zhang, N. Krishna, M.P. Lettinga, J. Vermant, E. Grelet, Langmuir **25**, 2437 (2009).
23. D.C. Morse, Macromolecules **31**, 7030 (1998).
24. D.C. Morse, Phys. Rev. E **63**, 031502 (2001).
25. J. Sambrook, E.F. Fritsch, T. Maniatis, *Molecular Cloning. A Laboratory Manual*, Vol. **1**, 2nd edition (Cold Spring Harbor Laboratory Press, EUA, 1989).
26. J. Galvan-Miyoshi, J. Delgado, R. Castillo, Eur. Phys. J. E **26**, 369 (2008).
27. D.A. Weitz, D.J. Pine, *Diffusing-Wave Spectroscopy*, in *Dynamic Light Scattering*, edited by W. Brown (Oxford University Press, New York, 1993) Chapt. 16, p. 652.
28. D.J. Pine, D.A. Weitz, J.X. Zhu, E. Herbolzheimer, J. Phys. (Paris) **51**, 2101 (1990).
29. D.D. Kaplan, M.H. Kao, A.G. Yodh, D.J. Pine, Appl. Opt. **32**, 3828 (1993).
30. T.D. Squires, T.G. Mason, Annu. Rev. Fluid Mech. **42**, 413 (2010).
31. M.L. Gardel, M.T. Valentine, D.A. Weitz, *Microrheology*, in *Microscale Diagnostic Techniques*, edited by K.S. Breuer (Springer, Berlin, 2005) Chapt. 1, p. 1.
32. T.G. Mason, D.A. Weitz, Phys. Rev. Lett. **74**, 1250 (1995).
33. T.G. Mason, Rheol. Acta **39**, 371 (2000).
34. J.H. van Zanten, K.P. Rufener, Phys. Rev. E **62**, 5389 (2000).
35. B.R. Dasgupta, S.Y. Tee, J.C. Crocker, B.J. Frisken, D.A. Weitz, Phys. Rev. E **65**, 51505 (2002).
36. M. Bellour, M. Skouri, J. P. Munch, P. Hebraud, Eur. Phys. J. E **8**, 431 (2002).
37. E. Sarmiento-Gomez, D. Lopez-Diaz, R. Castillo, J. Phys. Chem. B **114**, 3312193 (2010).
38. T.G. Mason, K. Ganesan, J.H. van Zanten, D. Wirtz, S.C. Kuo, Phys. Rev. Lett. **79**, 3282 (1997).
39. J. Galvan-Miyoshi, R. Castillo, Rev. Mex. Fis. **54**, 257 (2008).
40. L.F. Rojas-Ochoa, D. Lacoste, R. Lenke, P. Schurtenberger, F. Scheffold, J. Opt. Soc. Am. A **21**, 1799 (2004).
41. A. Ishimaru, *Wave Propagation and Scattering in Random Media* (Academic Press, New York, 1978).
42. H.C. van de Hulst, *Light Scattering by Small Particles* (Dover, New York, 1981).
43. Y.A. Wang, X. Yu, S. Overman, M. Tsuboi, G.J. Thomas, E. Egelman, J. Mol. Biol. **361**, 209 (2006).
44. S. Fraden, *Phase Transitions in Colloidal Suspensions of Virus Particles*, in *Observation, Prediction and Simulation of Phase Transitions in Complex Fluids*, edited by M. Baus, L.F. Rull, J.P. Ryckaert (Kluwer, Dordrecht, 1994) p. 113.
45. K.R. Purdy, *Liquid Crystal Phase Transitions of Monodisperse and Bidisperse Suspensions of Rodlike Colloidal Virus*, PhD Thesis, Brandeis University (2004).
46. R.G. Larson, Macromolecules **23**, 3983 (1990).
47. K. Kang, J. Gapinski, M.P. Lettinga, J. Buitenhuis, G. Meier, M. Ratajczyk, J.K.G. Dhont, A. Patkowski, J. Chem. Phys. **122**, 44905 (2005).
48. N. Willenbacher, C. Oelschlaeger, M. Schopferer, P. Fischer, Phys. Rev. Lett. **99**, 68302 (2007).